Separation and Purification Technology 379 (2025) 134409

Contents lists available at ScienceDirect

Separation and Purification Technology

journal homepage: www.elsevier.com/locate/seppur

Two-dimensional general rate model with particle size distribution in CADET calibrated with high-definition CFD simulated intra-column data

Jayghosh Subodh Rao [a,b], Samuel Leweke [a], Jan Michael Breuer [a,d], Stephan Menzel [e], Marek Behr [b,f], Eric von Lieres [a,c,f,*]

[a] Forschungszentrum Jülich, IBG-1: Biotechnology, 52428 Jülich, Germany
[b] RWTH Aachen University, Chair for Computational Analysis of Technical Systems (CATS), 52056 Aachen, Germany
[c] RWTH Aachen University, Computational Systems Biotechnology, 52074 Aachen, Germany
[d] University of Cologne, Faculty of Mathematics and Natural Sciences, Cologne, Germany
[e] GE Healthcare, Uppsala, Sweden
[f] JARA - Center for Simulation and Data Science, Germany

ARTICLE INFO

Communicated by Raquel Aires Barros

Keywords:
Column liquid chromatography
General rate model
Radial column gradients
Particle size distribution
High-definition simulation
CADET

ABSTRACT

Computational chromatography simulations mostly employ reduced-order models that simplify the intricate geometry of packed beds into one-dimensional representations. While computationally efficient, such models require extensive calibration as they lump the effects of packing heterogeneity, wall effects, and nonlinear flow and mass transport into dispersion coefficients and thin-film resistances at particle surfaces. To address these challenges, a two-dimensional extension of the general rate model was implemented in the open-source process simulator CADET. This study investigates the use of high-definition simulations as a source of reference data for calibrating both 1D and 2D general rate models with and without particle size distribution. Our results show that intra-column mass curves provide superior calibration data compared to conventional breakthrough curves. Consequently, properly calibrated reduced-order models can efficiently approximate polydisperse packings, even in thin columns with pronounced wall effects.

1. Introduction

A conventional packed-bed chromatography column constitutes a cylindrical container filled with a tightly but randomly packed bed of porous particles with functionally active inner surfaces. While the particles themselves are of simple geometries, their agglomeration in a packed bed results in a complex and tortuous interstitial space, also referred to as bulk or interparticle domain. Non-uniform packing density, particle morphology and size distribution, and packing defects are additional factors that increase the geometrical heterogeneity of the column. Additionally, the randomness of the packing is disrupted at the column walls, where a physical constraint is imposed on the particles and, consequently, the local porosity tends towards 1 after exhibiting an oscillatory pattern of increasing amplitude. Fluid flow in such a complex bulk region results in a highly non-linear velocity field, with hotspots where velocity can reach up to 10 times the average value, while simultaneously being slowed by friction at particle and wall surfaces. The resulting solute transport in the bulk domain is also non-uniform and highly tortuous. Further geometrical intricacies exist within the porous particles themselves in the form of macro- and micropores.

In modeling the chromatography process, it is convenient to assume homogeneity within the column and reduce it into a one-dimensional entity. Several conventional models of chromatography, such as the so-called general rate model (GRM), neglect the geometrical intricacies of the packed-bed and its effects on the flow field and solute concentration, and ascribe an average porosity and constant scalar velocity to the column. Although it is understood that the axial dispersion coefficients of these models account for molecular diffusion, eddy diffusion, and turbulence, Guiochon et al. [1], the effects of the above-mentioned geometrical inhomogeneities are inadvertently lumped into these coefficients. The resulting coefficients, while associated with a diffusive term, are orders of magnitude larger than the molecular diffusivity of the components in the solvent, even in columns with laminar flow. There are several popular reduced-order models (ROMs), in which effects of the thin boundary layer may be modeled using a film-diffusion coefficient separately, or also lumped into the axial dispersion coefficient. These models also neglect inhomogeneities in

* Corresponding author at: Forschungszentrum Jülich, IBG-1: Biotechnology, 52428 Jülich, Germany.
E-mail address: e.von.lieres@fz-juelich.de (E. von Lieres).

https://doi.org/10.1016/j.seppur.2025.134409
Received 29 April 2025; Received in revised form 17 July 2025; Accepted 18 July 2025
Available online 18 August 2025
1383-5866/© 2025 The Authors. Published by Elsevier B.V. This is an open access article under the CC BY license (http://creativecommons.org/licenses/by/4.0/).

particle loading, which are driven by the highly nonlinear velocity fields, causing large differentials in concentration values at different areas of the particle surfaces during the loading stage. The gains obtained with model simplicity, namely computational efficiency and reduced resource requirements, are offset by the need to calibrate the coefficients of these models using experimental data, usually breakthrough curves or other chromatograms. Such calibration processes only take into account the sensitivity of the estimated parameters to the difference between model prediction and reference data, ultimately reducing myriad inhomogeneities into their lumped dispersive effect on the predicted chromatogram. Calibrated ROMs are used in process design, optimization, and scale-up.

The dimensionality reduction in the column and particles, and the subsequent scalarization of porosity and velocity result in an inability of the model to capture variations in local porosity due to packing defects or wall effects. In particular, ROMs are unable to properly model very thin columns with relatively small column-to-particle radius ratios. The local porosity in a column may fluctuate substantially in these scenarios, with a value of 1 at column walls and tending towards an averaged porosity towards the column center. The rate of damping of the oscillations depends on the polydispersity of the packing, as smaller particles may nestle in the void spaces between larger ones, leading to a denser packing as compared to a purely monodisperse bed. This effect is minimal in typically used columns with a column-to-particle radius ratio $\frac{r_c}{r_p} \gg 10$, but can be significant in very thin microcolumns with large particle sizes. The radial profile of the interstitial velocity mostly follows that of local porosity, with the exception at particle and wall surfaces, where friction creates boundary layers in the flow field.

2D extensions of conventional ROMs enable modeling column properties in both the axial and radial dimensions. The increased model fidelity allows radial variations in local porosity and flowrates, making this class of models suitable in capturing wall effects and other column features which display radial variability. Numerical implementations of these models effectively discretize the column into N_ρ concentric zones, across which mass transfer is modeled via radial dispersion terms. While they are computationally more expensive, being mere dimensional extensions of conventional models, 2D ROMs are still relatively simple to set up and execute. However, these apparent benefits are completely overshadowed by the increase in number of lumped parameters that require tuning. In the 2D GRM, for instance, both the axial and radial dispersion coefficients may vary in each radial discretization zone of the column, resulting in a set of $2N_\rho$ dispersion parameters that characterize the column. The necessary increase in spatial resolution in reference data can experimentally be achieved using techniques such as confocal laser scanning microscopy (CLSM) [2,3] which, however, strongly restrict the types of columns and solutes that may be used.

High definition (HD) models of chromatography take into account the complete 3D macroscopic geometry of the column and offer unique insights into the flow and transport processes within the column. The interparticle geometry is fully resolved, while the intraparticle geometry is assumed to be homogeneous, i.e., particle shapes are resolved, but not particle pores. These mechanistic models are much more detailed than the GRM since dispersion inherently appears as a consequence of simulating the flow and transport in realistic and tortuous interstitial geometries. The mass transfer resistance at particle surfaces are also modeled inherently due to flow boundary layers that are caused by friction between the fluid and particle surfaces. The cost of such 3D models is the mathematical and computational complexity coupled with immense computational resources required to develop and deploy these models and their tooling. HD models require further development and performance improvements before they can simulate even relatively small lab-scale columns. However, due to the mechanistic nature of these simulations, the spatially resolved results are perfectly suited to be used as reference data for calibrating ROMs of varying configurations, which can then be scaled up at substantially lower costs.

In this work, we demonstrate the utility of HD simulations as reference data for calibrating 1D and 2D ROMs. The ultimate goal of the overarching project is to expand on this concept and resolve the effects of various geometrical features and interstitial phenomena on reduced-order model coefficients.

In the following sections of this paper, we first showcase the implementation details of the 2D GRM in CADET-Core (https://github.com/cadet/CADET-Core), an open-source reduced-order process simulator. We also describe further extensions to both the 1D and 2D GRM that enable modeling particle size distributions (PSDs) in ROMs of packed bed liquid chromatography. Next, simulation setup and ROM calibration strategy based on reference data from HD simulations are introduced with a numerical case study. Finally, calibration results are shown and discussed, before conclusions are drawn and an outlook is presented.

2. General rate model extensions

The classic GRM can be considered a blueprint from which other chromatography models are derived [1]. For example, the lumped rate model with pores (LRMP) or the lumped rate model without pores (LRM) are reduced-order versions of the GRM in which pore diffusion or the entire pore phase are neglected. The following formulation of the GRM, as implemented in CADET-Core prior to the extensions introduced in this work, is presented as the base case from which our extensions are derived.

2.1. Classic general rate model (GRM)

We here introduce a version of the GRM that includes pore and surface diffusion, Eq. (1). Binding can be described by various models, such as the Langmuir model.

$$F_i^b = -\beta^b \frac{\partial c_i^b}{\partial t} - \beta^b u \frac{\partial c_i^b}{\partial z} + \beta^b D_{\mathrm{ax},i} \frac{\partial^2 c_i^b}{\partial z^2} - \beta^p j_{f,i} \tag{1a}$$

$$F_i^p = -\beta^p \frac{\partial c_i^p}{\partial t} + \beta^p D_{p,i} \left(\frac{\partial^2 c_i^p}{\partial r^2} + \frac{2}{r} \frac{\partial c_i^p}{\partial r} \right) - \beta^s j_{b,i} \tag{1b}$$

$$F_i^s = -\beta^s \frac{\partial c_i^s}{\partial t} + \beta^s D_{s,i} \left(\frac{\partial^2 c_i^s}{\partial r^2} + \frac{2}{r} \frac{\partial c_i^s}{\partial r} \right) + \beta^s j_{b,i} \tag{1c}$$

For later convenience, the model equations are written in implicit form, $F_i^\kappa = 0$, and all concentrations are denoted by c_i^κ. The index $\kappa \in \{b, p, s\}$ indicates the phase, namely b for the bulk or interstitial volume, p for the particle pores and s for the stationary phase. The phase ratios $\beta^b = \varepsilon_c$, $\beta^p = (1-\varepsilon_c)\varepsilon_p$ and $\beta^s = (1-\varepsilon_c)(1-\varepsilon_p)$, where ε_c and ε_p are the column and particle porosities, are introduced for harmonizing the units of F_i^b, F_i^p and F_i^s. In Eq. (1), i indicates the species or component, $D_{\mathrm{ax},i}$ is the axial dispersion coefficient, $D_{p,i}$ and $D_{s,i}$ are the pore and surface diffusion coefficients, and is u the interstitial velocity. Moreover, T denotes total simulation time and L column length, $t \in [0, T]$ and $z \in [0, L]$ are the time and axial coordinates.

The flux $j_{f,i}$ describes the transfer of solute molecules between the interstitial volume and the particle pores by film diffusion, with a mass transfer coefficient $k_{f,i}$ and particle radius $r_p \ll L$, Eq. (2).

$$j_{f,i} = \frac{1}{\varepsilon_p} \frac{3}{r_p} k_{f,i} \left(c_i^b - c_i^p(r = r_p) \right) \tag{2}$$

The flux $j_{b,i}$ describes the transfer of solute molecules between the pore phase and the stationary phase by adsorption and desorption. The presented modeling framework can technically be combined with any binding model that can be written as differential–algebraic equation, for example the Langmuir model [4], Eq. (3), with adsorption and desorption rates $k_{a,i}$ and $k_{d,i}$, maximal binding capacity $c^s_{\mathrm{max},i}$. N_c denotes the number of components.

$$j_{b,i} = k_{a,i} c_i^p c^s_{\mathrm{max},i} \left(1 - \sum_{j=1}^{N_c} \frac{c_j^s}{c^s_{\mathrm{max},j}} \right) - k_{d,i} c_i^s \tag{3}$$

Danckwerts boundary conditions [5], Eq. (4), are used at the column inlet and outlet.

$$-u\,c_i^b(z=0)+D_{\mathrm{ax}}\frac{\partial c_i^b}{\partial z}(z=0)=-u\,c_{\mathrm{in},i}^b \tag{4a}$$

$$\frac{\partial c_i^b}{\partial z}(z=L)=0 \tag{4b}$$

Further boundary conditions are required at the particle center and surface, Eq. (5).

$$D_{p,i}\frac{\partial c_i^p}{\partial r}(r=0)=0 \qquad \text{and} \qquad D_{s,i}\frac{\partial c_i^s}{\partial r}(r=0)=0 \tag{5a}$$

$$\frac{3}{r_p}D_{p,i}\frac{\partial c_i^p}{\partial r}(r=r_p)=j_{f,i} \qquad \text{and} \qquad \frac{3}{r_p}D_{s,i}\frac{\partial c_i^s}{\partial r}(r=r_p)=0 \tag{5b}$$

The binding process can also be treated in rapid equilibrium. In this case, only the equilibrium constants, $k_{\mathrm{eq},i}=\frac{k_{a,i}}{k_{d,i}}$, need to be known instead of the adsorption and desorption constants. Moreover, mathematically overdetermined systems need to be avoided by setting up the transport equations only for conserved moieties. These are the sum of particle pore and stationary phase concentrations, as referred to the total column volume, $\beta^p c_i^p+\beta^s c_i^s$. The binding model is used for closing the remaining degrees of freedom. When the binding process of all components is treated in rapid equilibrium, the GRM in Eq. (1) with boundary conditions in Eq. (5) takes the form given in Eq. (6) with boundary conditions in Eq. (7).

$$F_i^b=-\beta^b\frac{\partial c_i^b}{\partial t}-\beta^b u\frac{\partial c_i^b}{\partial z}+\beta^b D_{\mathrm{ax},i}\frac{\partial^2 c_i^b}{\partial z^2}-\beta^p j_{f,i} \tag{6a}$$

$$F_i^p+F_i^s=-\beta^p\frac{\partial c_i^p}{\partial t}+\beta^p D_{p,i}\left(\frac{\partial^2 c_i^p}{\partial r^2}+\frac{2}{r}\frac{\partial c_i^p}{\partial r}\right)-\beta^s\frac{\partial c_i^s}{\partial t}+\beta^s D_{s,i}\left(\frac{\partial^2 c_i^s}{\partial r^2}+\frac{2}{r}\frac{\partial c_i^s}{\partial r}\right) \tag{6b}$$

$$j_{b,i}=0 \tag{6c}$$

$$\beta^p D_{p,i}\frac{\partial c_i^p}{\partial r}(r=0)+\beta^s D_{s,i}\frac{\partial c_i^s}{\partial r}(r=0)=0 \tag{7a}$$

$$\beta^p\frac{3}{r_p}D_{p,i}\frac{\partial c_i^p}{\partial r}(r=r_p)+\beta^s\frac{3}{r_p}D_{s,i}\frac{\partial c_i^s}{\partial r}(r=r_p)=\beta^p j_{f,i} \tag{7b}$$

2.2. Two-dimensional general rate model (2D GRM)

In the 2D GRM, the concentrations also depend on the radial coordinate of the column, $\rho\in[0,r_c]$ where r_c is the column radius [6]. In addition, the particle volume fractions d_j, the column porosity ε_c, flow velocity u, and the axial and radial dispersion coefficients $D_{\mathrm{ax},i}$, $D_{\rho,i}$ may depend on the radial coordinate.

$$F_i^b=-\beta^b\frac{\partial c_i^b}{\partial t}-\beta^b u\frac{\partial c_i^b}{\partial z}+\beta^b D_{\mathrm{ax},i}\frac{\partial^2 c_i^b}{\partial z^2}+\frac{1}{\rho}\frac{\partial}{\partial\rho}\left(D_{\rho,i}\rho\frac{\partial}{\partial\rho}\left(\beta^b c_i^b\right)\right)-\beta^p j_{f,i} \tag{8}$$

Danckwerts boundary conditions Eq. (4) are imposed on the axial boundaries, where the inlet profile can also change in the radial direction. Additional boundary conditions at the column center and wall are:

$$\frac{\partial c_i^b}{\partial\rho}(\rho=0)=0 \tag{9a}$$

$$\frac{\partial c_i^b}{\partial\rho}(\rho=r_c)=0 \tag{9b}$$

2.3. Particle size distribution (PSD)

A PSD can be modeled by setting up several instances of the particle model with individual radii and adjusting the boundary fluxes between the interstitial volume and these representative particles [7].[1] Consider a discrete distribution of $j=1,\dots,N_p$ particle sizes, where d_j is the volume fraction of particles with radius $r_{p,j}$, i.e., $\sum_{j=1}^{N_p}d_j=1$. Eqs. (1b)–(1c), (2)–(3) and (5) are individually set up for each of the representative particles with index j. All parameters, including particle porosity, ε_p, and the film mass transfer coefficient, $k_{f,i}$, even the binding parameters can depend on j.

$$F_i^b=-\beta^b\frac{\partial c_i^b}{\partial t}-\beta^b u\frac{\partial c_i^b}{\partial z}+\beta^b D_{\mathrm{ax},i}\frac{\partial^2 c_i^b}{\partial z^2}+\frac{1}{\rho}\frac{\partial}{\partial\rho}\left(D_{\rho,i}\rho\frac{\partial}{\partial\rho}\left(\beta^b c_i^b\right)\right)-\sum_{j=1}^{N_p}\beta_j^p d_j j_{f,i,j} \tag{10}$$

3. Spatial discretization

3.1. Classic general rate model (GRM)

The GRM, Eq. (1), constitutes a system of non-linear partial differential–algebraic equations (PDAE). These equations are first discretized in the spatial domain using finite volumes (FV), resulting in a large system of non-linear ordinary differential equations (DAE). The residuals, F_i^b, interstitial concentrations, c_i^b, and boundary fluxes, $j_{f,i}$, are spatially averaged in $p=1,\dots,N_z$ uniform cells with $\Delta z=\frac{L}{N_z}$. In Eq. (11), $z_{p-\frac{1}{2}}=(p-1)\Delta z$ and $z_{p+\frac{1}{2}}=p\Delta z$ denote the left and right cell boundaries, and the axial cell centers are given by $z_p=(p-\frac{1}{2})\Delta z$.

$$\bar{F}_i^b(p,t)=\frac{1}{\Delta z}\int_{z_{p-\frac{1}{2}}}^{z_{p+\frac{1}{2}}}F_i^b(z,t)\,\mathrm{d}z \tag{11a}$$

$$\bar{c}_i^b(p,t)=\frac{1}{\Delta z}\int_{z_{p-\frac{1}{2}}}^{z_{p+\frac{1}{2}}}c_i^b(z,t)\,\mathrm{d}z \tag{11b}$$

$$\bar{j}_{f,i}(p,t)=\frac{1}{\Delta z}\int_{z_{p-\frac{1}{2}}}^{z_{p+\frac{1}{2}}}j_{f,i}(z,t)\,\mathrm{d}z \tag{11c}$$

Representative beads at the centers z_p of the axial cells are radially discretized. The residuals, F_i^κ, mobile and stationary phase concentrations, c_i^κ, with $\kappa\in\{p,s\}$ and the binding fluxes, $j_{b,i}$, are spatially averaged in $q=1,\dots,N_r$ spherical shells with $\Delta r=\frac{r_p}{N_r}$, Eq. (12).

$$\bar{F}_i^\kappa(p,q,t)=\frac{1}{V_q}\int_{r_{q+\frac{1}{2}}}^{r_{q-\frac{1}{2}}}F_i^\kappa(z_p,r,t)A(r)dr \quad \text{with} \quad \kappa\in\{p,s\} \tag{12a}$$

$$\bar{c}_i^\kappa(p,q,t)=\frac{1}{V_q}\int_{r_{q+\frac{1}{2}}}^{r_{q-\frac{1}{2}}}c_i^\kappa(z_p,r,t)A(r)dr \quad \text{with} \quad \kappa\in\{p,s\} \tag{12b}$$

$$\bar{j}_{b,i}(p,q,t)=\frac{1}{V_q}\int_{r_{q+\frac{1}{2}}}^{r_{q-\frac{1}{2}}}j_{b,i}(z_p,r,t)A(r)dr \tag{12c}$$

Note that the radial cells are numbered in ascending order from bead surface to center. Here $r_{q-\frac{1}{2}}=r_p-(q-1)\Delta r$ and $r_{q+\frac{1}{2}}=r_p-q\Delta r$ denote the outer and inner cell boundaries. The radial cell centers are given by $r_q=r_p-(q-\frac{1}{2})\Delta r$, V_q are the corresponding cell volumes, Eq. (13a), and $A(r)$ is the surface area of a sphere with radius r, Eq. (13b).

$$V_q=\frac{4\pi}{3}\left(r_{q-\frac{1}{2}}^3-r_{q+\frac{1}{2}}^3\right) \tag{13a}$$

$$A(r)=4\pi r^2 \tag{13b}$$

The interstitial mass balances, Eq. (1a), are integrated over each cell and divided by Δz, Eq. (14a), and the bead mass balances, Eq. (1b)–(1c),

[1] Equivalence with Eq. (4) in [7] can be verified by neglecting convection and dispersion in Eq. (8), inserting the outer particle boundary condition, Eq. (5), and using the definitions of the column and particle porosities, $\varepsilon_c=\frac{V^b}{V^b+V^p+V^s}$ and $\varepsilon_p=\frac{V^p}{V^p+V^s}$.

are multiplied by the area, $A(r)$, integrated over each cell and divided by the respective volumes V_q, Eq. (14b).

$$\bar{F}_i^b = -\beta^b \frac{\partial \bar{c}_i^b}{\partial t} - \beta^b u \frac{c_i^b(z = z_{p+\frac{1}{2}}) - c_i^b(z = z_{p-\frac{1}{2}})}{\Delta z} + \beta^b D_{\mathrm{ax},i} \frac{\frac{\partial c_i^b}{\partial z}(z = z_{p+\frac{1}{2}}) - \frac{\partial c_i^b}{\partial z}(z = z_{p-\frac{1}{2}})}{\Delta z} - \beta^p \bar{j}_{f,i} \tag{14a}$$

$$\bar{F}_i^p = -\beta^p \frac{\partial \bar{c}_i^p}{\partial t} + \beta^p D_{p,i} \frac{A(r_{q-\frac{1}{2}})}{V_q} \frac{\partial c_i^p}{\partial r}(z = z_p, r = r_{q-\frac{1}{2}}) - \beta^p D_{p,i} \frac{A(r_{q+\frac{1}{2}})}{V_q} \frac{\partial c_i^p}{\partial r}(z = z_p, r = r_{q+\frac{1}{2}}) - \beta^s \bar{j}_{b,i} \tag{14b}$$

$$\bar{F}_i^s = -\beta^s \frac{\partial \bar{c}_i^s}{\partial t} + \beta^s D_{s,i} \frac{A(r_{q-\frac{1}{2}})}{V_q} \frac{\partial c_i^s}{\partial r}(z = z_p, r = r_{q-\frac{1}{2}}) - \beta^s D_{s,i} \frac{A(r_{q+\frac{1}{2}})}{V_q} \frac{\partial c_i^s}{\partial r}(z = z_p, r = r_{q+\frac{1}{2}}) + \beta^s \bar{j}_{b,i} \tag{14c}$$

The boundary concentrations, c_i^b, are accurately reconstructed from cell averages using a weighted essentially non-oscillatory (WENO) scheme, as described by Lieres and Andersson [8]. The spatial derivatives of the boundary concentrations, $\frac{\partial c_i^b}{\partial z}$, $\frac{\partial c_i^p}{\partial r}$ and $\frac{\partial c_i^s}{\partial r}$, are estimated from adjacent cell averages. They are approximated by symmetric first order differences, Eq. (15).

$$\frac{\partial c_i^b}{\partial z}(z_{p+\frac{1}{2}}, t) \approx \frac{\bar{c}_i^b(p+1,t) - \bar{c}_i^b(p,t)}{\Delta z} \tag{15a}$$

$$\frac{\partial c_i^b}{\partial z}(z_{p-\frac{1}{2}}, t) \approx \frac{\bar{c}_i^b(p,t) - \bar{c}_i^b(p-1,t)}{\Delta z} \tag{15b}$$

$$\frac{\partial c_i^\kappa}{\partial r}(z_p, r_{q-\frac{1}{2}}, t) \approx \frac{\bar{c}_i^\kappa(p,q-1,t) - \bar{c}_i^\kappa(p,q,t)}{\Delta r} \quad \text{with} \quad \kappa \in \{p,s\} \tag{15c}$$

$$\frac{\partial c_i^\kappa}{\partial r}(z_p, r_{q+\frac{1}{2}}, t) \approx \frac{\bar{c}_i^\kappa(p,q,t) - \bar{c}_i^\kappa(p,q+1,t)}{\Delta r} \quad \text{with} \quad \kappa \in \{p,s\} \tag{15d}$$

The column and particle boundary conditions naturally enter the finite volume scheme. According to Eq. (4) the terms $-u\, c_i^b(z = z_{\frac{1}{2}}) + D_{ax,i} \frac{\partial c_i^b}{\partial z}(z = z_{\frac{1}{2}})$ in the first cell average are substituted by $-u\, c_{in,i}^b$ and the term $\frac{\partial c_i^b}{\partial z}(z = z_{N_z+\frac{1}{2}})$ in the last cell average is zero. According to Eq. (5), the terms $\frac{\partial c_i^p}{\partial r}(z = z_p, r = r_{N_r+\frac{1}{2}})$, $\frac{\partial c_i^s}{\partial r}(z = z_p, r = r_{\frac{1}{2}})$ and $\frac{\partial c_i^s}{\partial r}(z = z_p, r = r_{N_r+\frac{1}{2}})$ are also zero.

Accurate handling of the term $\frac{\partial c_i^p}{\partial r}(z = z_p, r = r_{\frac{1}{2}})$ in the outermost cell average requires a little more effort. First, the boundary flux, Eq. (2), is inserted in the original boundary condition, Eq. (5). Eq. (16) is obtained by considering $r_p = r_{\frac{1}{2}}$.

$$\frac{\varepsilon_p D_{p,i}}{k_{f,i}} \frac{\partial c_i^p}{\partial r}(r = r_{\frac{1}{2}}) = c_i^b - c_i^p(r = r_{\frac{1}{2}}) \tag{16}$$

Then, the spatial derivative in Eq. (16) is approximated by a finite difference.

$$\frac{\varepsilon_p D_{p,i}}{k_{f,i}} \frac{c_i^p(r = r_{\frac{1}{2}}) - c_i^p(r = r_1)}{r_{\frac{1}{2}} - r_1} = c_i^b - c_i^p(r = r_{\frac{1}{2}}) \tag{17}$$

Now, Eq. (16) is solved for $c_i^p(r = r_{\frac{1}{2}})$.

$$c_i^p(r = r_{\frac{1}{2}}) = c_i^b - \frac{\varepsilon_p D_{p,i}}{k_{f,i}} \frac{\partial c_i^p}{\partial r}(r = r_{\frac{1}{2}}) \tag{18}$$

The result is inserted in Eq. (17).

$$\frac{c_i^b - \frac{\varepsilon_p D_{p,i}}{k_{f,i}} \frac{\partial c_i^p}{\partial r}(r = r_{\frac{1}{2}}) - c_i^p(r = r_1)}{r_{\frac{1}{2}} - r_1} = \frac{\partial c_i^p}{\partial r}(r = r_{\frac{1}{2}}) \tag{19}$$

Eq. (19) is then solved for $\frac{\partial c_i^p}{\partial r}(r = r_{\frac{1}{2}})$.

$$\frac{\partial c_i^p}{\partial r}(r = r_{\frac{1}{2}}) = \frac{c_i^b - c_i^p(r = r_1)}{r_{\frac{1}{2}} - r_1 + \frac{\varepsilon_p D_{p,i}}{k_{f,i}}} \tag{20}$$

Finally, the interstitial and pore phase concentrations, c_i^b and c_i^p, in the cell centers, $z = z_p$ and $r = r_1$, are approximated by their respective cell averages, $\bar{c}_i^b$ and $\bar{c}_i^p$.

$$\frac{\partial c_i^p}{\partial r}(z = z_p, r = r_{\frac{1}{2}}) = \frac{\bar{c}_i^b(z = z_p) - \bar{c}_i^p(z = z_p, r = r_1)}{r_{\frac{1}{2}} - r_1 + \frac{\varepsilon_p D_{p,i}}{k_{f,i}}} \tag{21}$$

Eq. (21) is used for substituting $\frac{\partial c_i^p}{\partial r}(z = z_p, r = r_{\frac{1}{2}})$ in Eq. (14b) in the outermost radial cell. Moreover, it is inserted in Eq. (5) for computing the boundary flux, $\bar{j}_{f,i}$.

$$\bar{j}_{f,i} = \frac{1}{\varepsilon_p} \frac{3}{r_p} \bar{k}_{f,i} \left(\bar{c}_i^b - \bar{c}_i^p(r = r_1)\right) \quad \text{with} \quad \bar{k}_{f,i} = \frac{1}{\frac{1}{k_{f,i}} + \frac{r_{\frac{1}{2}} - r_1}{\varepsilon_p D_{p,i}}} \tag{22}$$

The binding model is analogously set up for the averaged concentrations.

$$\bar{j}_{b,i} = k_{a,i} \bar{c}_i^p c_{\max,i}^s \left(1 - \sum_{j=1}^{N_c} \frac{\bar{c}_j^s}{c_{\max,j}^s}\right) - k_{d,i} \bar{c}_i^s \tag{23}$$

3.2. Two-dimensional general rate model (2D GRM)

We discretize the 2D transport Eq. (8) using a suitable FV method. To achieve this, we make the following simplifying assumption, which reduces the complexity of the model: Parameters that depend on the radial position are assumed to be piecewise constant. Specifically, the column can be partitioned into $N_\rho \in \mathbb{N}$ radial zones in which particle volume fractions and porosity, velocity and dispersion parameters remain constant in radial direction. In the following, we use the radial zones as boundaries for the finite volume (FV) cells, while allowing parameters to remain constant across neighboring FV cells. Discontinuities of the piecewise constant parameters always coincide with FV cell interfaces; however, not every interface corresponds to a discontinuity. Refinement of the FV grid is achieved by subdividing the existing FV cells.

In addition to discretizing the axial column coordinate into N_z uniform cells of size $\Delta z = \frac{L}{N_z}$, the radial column coordinate is divided into N_ρ cells, which can have non-uniform sizes:

$$0 = \rho_{1/2} < \rho_{3/2} < \cdots < \rho_{N_\rho+1/2} = r_c. \tag{24}$$

A cell with inner radius $\rho_{w-1/2}$ and outer radius $\rho_{w+1/2}$ has its center at $\rho_w = (\rho_{w+1/2} + \rho_{w-1/2})/2$ for $w = 1, \ldots, N_\rho$. Its radial extension is denoted by $\Delta\rho_w = \rho_{w+1/2} - \rho_{w-1/2}$. Each cylinder shell with length Δz has a volume V_w':

$$V_w' = \pi \left(\rho_{w+\frac{1}{2}}^2 - \rho_{w-\frac{1}{2}}^2\right) \Delta z = 2\pi \rho_w \Delta\rho_w \Delta z. \tag{25}$$

The discretization and domain coupling in 2D GRM is illustrated in Fig. 1.

Integrating the interstitial concentrations c_i^b and the bead fluxes $j_{f,i}$ over cylinder shells and dividing by their respective volume, we obtain the averaged moieties:

$$\bar{F}_i^b(p,w,t) = \frac{2\pi}{V_w'} \int_{\rho_{w-\frac{1}{2}}}^{\rho_{w+\frac{1}{2}}} \int_{z_{p-\frac{1}{2}}}^{z_{p+\frac{1}{2}}} F_i^b(z,\rho,t)\, \mathrm{d}z\, \rho\, \mathrm{d}\rho \tag{26a}$$

$$\bar{c}_i^b(p,w,t) = \frac{2\pi}{V_w'} \int_{\rho_{w-\frac{1}{2}}}^{\rho_{w+\frac{1}{2}}} \int_{z_{p-\frac{1}{2}}}^{z_{p+\frac{1}{2}}} c_i^b(z,\rho,t)\, \mathrm{d}z\, \rho\, \mathrm{d}\rho \tag{26b}$$

$$\bar{j}_{f,i}(p,w,t) = \frac{2\pi}{V_w'} \int_{\rho_{w-\frac{1}{2}}}^{\rho_{w+\frac{1}{2}}} \int_{z_{p-\frac{1}{2}}}^{z_{p+\frac{1}{2}}} j_{f,i}(z,\rho,t)\, \mathrm{d}z\, \rho\, \mathrm{d}\rho \tag{26c}$$

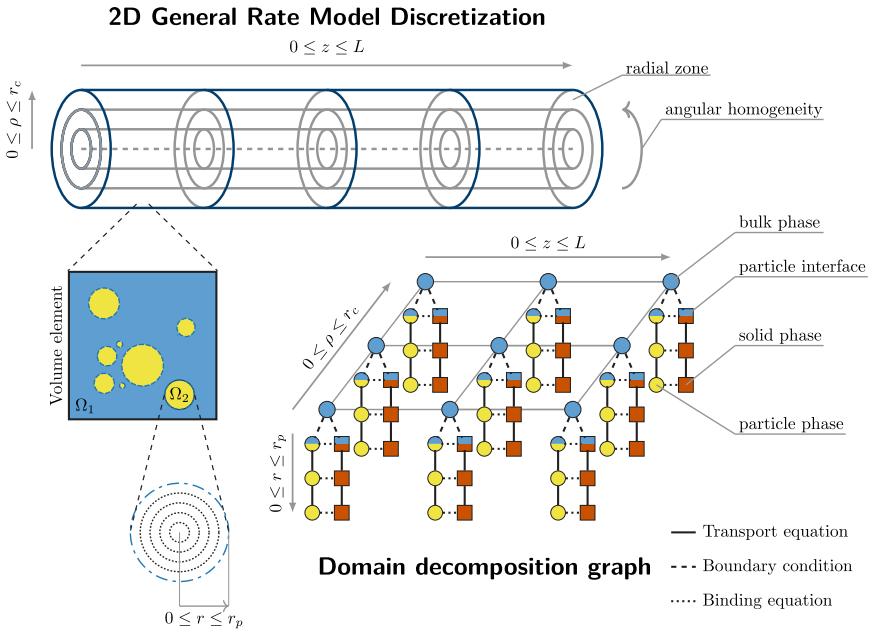

Fig. 1. Discretization and domain decomposition in 2D GRM.

Note that we have

$$\bar{c}_i^b(p,w,t) = c_i^b\left(z_p, \rho_w, t\right) + O\left((\Delta z)^2 + \left(\Delta\rho_w\right)^2\right)$$

for sufficiently smooth functions c_i^b. Concluding, these volume averages are suitable approximations of the function value at the corresponding cell centers.

Further derivation of the numerical discretization along with implementation details can be found in the supplement.

3.3. Particle size distributions (PSD)

Spatial discretization of the GRM with PSD is straightforward.

$$\begin{aligned}\bar{F}_i^b =& -\beta^b \frac{\partial \bar{c}_i^b}{\partial t} - \beta^b u \frac{c_i^b(z = z_{p+\frac{1}{2}}) - c_i^b(z = z_{p-\frac{1}{2}})}{\Delta z} \\ &+ \beta^b D_{\mathrm{ax},i} \frac{\frac{\partial c_i^b}{\partial z}(z = z_{p+\frac{1}{2}}) - \frac{\partial c_i^b}{\partial z}(z = z_{p-\frac{1}{2}})}{\Delta z} - \sum_{j=1}^{N_p} \beta_j^p d_j \bar{J}_{f,i,j}\end{aligned} \tag{27}$$

For the 2D extension in eq. (S1), we similarly obtain

$$\begin{aligned}\bar{F}_i^b(p,w,t) =& -\beta^b\left(\rho_w\right) \frac{\partial \bar{c}_i^b(p,w,t)}{\partial t} - \sum_{j=1}^{N_p} \beta_j^p\left(\rho_w\right) d_j\left(\rho_w\right) \bar{J}_{f,i,j}(p,w,t) \\ &+ \frac{2\pi}{V_w'} \int_{\rho_{w-\frac{1}{2}}}^{\rho_{w+\frac{1}{2}}} \beta^b \left[-u\, c_i^b(z,\rho,t) + D_{\mathrm{ax},i} \frac{\partial c_i^b}{\partial z}(z,\rho,t)\right]_{z_{p-\frac{1}{2}}}^{z_{p+\frac{1}{2}}} \rho \,\mathrm{d}\rho \\ &+ \frac{2\pi}{V_w'} \int_{z_{p-\frac{1}{2}}}^{z_{p+\frac{1}{2}}} \left[\rho D_{\rho,i} \beta^b \frac{\partial c_i^b}{\partial \rho}(z,\rho,t)\right]_{\rho_{w-\frac{1}{2}}}^{\rho_{w+\frac{1}{2}}} \mathrm{d}z.\end{aligned} \tag{28}$$

Note that, in addition to the porosities, we also allow the particle size distribution d_j to depend on the radial position in the column bulk volume.

4. CADET implementation and verification

4.1. 2D GRM implementation details

CADET-Core, the C++ numerical engine in the CADET project, is published as open source software on GitHub under the GPL 3.0 license [9]. To integrate the semi-discrete DAE system derived in Section 3 in time, we use the backwards-differentiation formula (BDF) implemented in the IDAS module of SUNDIALS [10,11]. This BDF implementation can solve DAE systems of differential index 1 and is well suited for stiff problems, which commonly occur in chromatography due to, e.g., non-linear binding and reaction mechanisms. Based on years of experience with IDAS, we have found this method and its implementation to be highly robust and stable. The time integrator uses a Newton method to solve the linear system of the fully discretized system and thus requires the system Jacobian

$$J = \frac{\partial F}{\partial y}, \tag{29}$$

where $F : \mathbb{R}^n \mapsto \mathbb{R}^n$ is the residual function of the semi-discrete system. The Jacobian is very sparse and we employ a specific order to the state vector (see Section S1 in the supplement) to achieve an arrowhead Jacobian structure, see Eq. (S13). This favorable structure is exploited by our custom linear solver module, which is based on a Schur LU factorization into upper and lower block triangular matrices [8]. The specific Jacobian blocks are shown in Section S2 in the supplement, and the global Jacobian was verified through compressed algorithmic differentiation (AD) as described by Püttmann et al. [12].

Furthermore, our 1D and 2D GRM implementations support parameter sensitivity estimation, leveraging the capabilities provided by IDAS to compute sensitivities using the forward method, combined with AD, as described by Püttmann et al. [13].

4.2. 2D GRM verification

Verification and validation are fundamental in modeling and simulation. Verification is focused on the mathematical methods and their implementation to confirm their correctness. Validation examines the model itself, assessing whether it effectively addresses domain-specific, real-world problems and represents the underlying physics with sufficient accuracy. Since verification forms the foundation for reliable validation, it is a prerequisite and is addressed first; the subsequent Sections 5 and 6 are focused on validation.

To verify the implementation of the 2D GRM and FV the discretization derived in Section 3.2, we conduct order-of-accuracy tests, which are widely considered the most reliable and rigorous tests for numerical

Table 1
Convergence table for the 2D GRM with four particle types and three radial zones discretizing radial inhomogeneity. The number of FV cells in axial, radial and particle direction are denoted by N_e^z, N_e^r, N_e^p, respectively. Model parameters are shown in Table S6.

N_e^z	N_e^r	N_e^p	Max. error	Max. EOC	L^2 error	L^2 EOC	Bulk DoF
4	3	3	$7.94 \cdot 10^{-2}$	0.0	$4.73 \cdot 10^{-1}$	0.0	12
8	6	6	$1.66 \cdot 10^{-2}$	2.26	$1.50 \cdot 10^{-1}$	1.66	48
16	12	12	$4.15 \cdot 10^{-3}$	2.00	$4.38 \cdot 10^{-2}$	1.78	192
32	24	24	$1.01 \cdot 10^{-3}$	2.04	$1.11 \cdot 10^{-2}$	1.98	768
64	48	48	$2.36 \cdot 10^{-4}$	2.10	$2.66 \cdot 10^{-3}$	2.06	3072

simulation software. To this end, we compute an experimental order of convergence (EOC) for the kth refinement of the spatial grid

$$EOC_k = \frac{\ln(\text{error}_k) - \ln(\text{error}_{k-1})}{\ln(h_{k-1}) - \ln(h_k)}, \tag{30}$$

where $\text{error}_k \in \mathbb{R}$ is some error metric for the kth approximation, and $h_k \in \mathbb{N}$ is the number of FV cells in axial direction. We note that the discretization must be refined at the same rate for all spatial directions, see e.g. Table 1. To pass the test, the EOC must converge asymptotically to the theoretical order of convergence, which is 2 for our FV scheme (2th order method). We note our FV scheme only exhibits a theoretical convergence order 2, if we define radial zones in which the parameters, such as porosity, are constant w.r.t their spatial position. Thus, to verify the second order convergence via EOC tests, we define three radial zones which are discretized by the same number of radial FV cells, which are equally refined.

To further strengthen the test, we assess the convergence towards an analytical solution. To this end, we extended CADET-Semi-Analytic [14,15] by a Hankel–Laplace domain solution of the two-dimensional general rate model with linear binding, following the work of Qamar et al. [6]. We note that the available analytical solutions are limited to linear bindings and constant velocity and dispersion parameters.

To model radial inhomogeneity, we define three radial zones which are fed with different concentrations. For the most extensive setting we employ four particle types, with varying fraction of the solid volume in each zone. Another setting solely considers the bulk transport, i.e. molecules cannot enter the particles, to separately test the FV discretization of the two-dimensional interstitial volume equation. We further consider a setting involving a single particle type but with different modes: kinetic binding, rapid-equilibrium binding, and scenarios with or without surface diffusion. The parameters for all six settings are given in Table S6, the convergence results are given in Table 1 and in the supplement, Tables S1–S5.

To assess the convergence of our discretized model, we consider the discrete maximum norm of the L^∞ and L^2 error of the approximations over all radial zones at the column outlet; see for reference Table 1. The evaluation code for software verification, including model setups and convergence analysis, is publicly available in the CADET-Verification test suite [16].

Second order convergence is clearly achieved for all settings and the methods and implementation thus pass the order-of-accuracy test. Furthermore, CADET-Core and CADET-Semi-Analytic mutually verified each other. The code specifically configured for this verification study is publicly available on GitHub as part of the CADET verification and testing pipeline.

5. ROM calibration case study

Fig. 2 schematically illustrates the ROM calibration workflow based on reference HD simulations developed in this work in the context of a 2D GRM. This workflow comprises performing the reference HD simulation, configuring the ROM simulation to be calibrated, and the parameter estimation process. The optimization loop, central to the parameter estimation process, iteratively updates ROM calibration parameters in the ROM simulation based on the residuals of objective

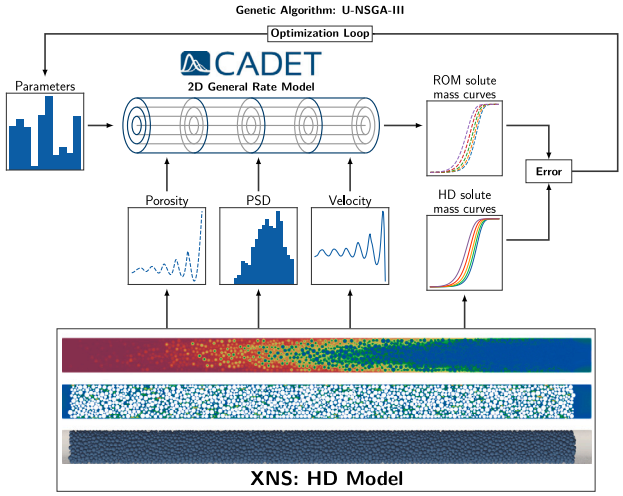

Fig. 2. ROM calibration workflow.

functions, which operate on ROM outputs (predictions) and HD reference data pertaining to selected column characteristics (objectives). The following subsections describe these elements in detail.

An open-source calibration tool, chromoo [17], that interfaces with CADET-Core for ROM evaluations and uses pymoo [18] as the underlying optimization framework was specifically developed for this work.

5.1. HD simulation setup and reference data

The column setup and HD simulations from a previous study [19] were used as reference for this work. Two hypothetical microcolumns of equal lengths, widths, and total bed capacities, but differing packing morphologies were analyzed: One featuring a monodisperse packing of 13,845 particles, and the other a polydisperse packing of 9874 particles. The packings were numerically generated by the Tallarek group at Philipps-University, Marburg using a modified Jodrey–Tory algorithm [20,21]. To account for a slightly higher packing density of the polydisperse packing, its bed length was adjusted to ensure equal bed capacities and average column porosities relative to the monodisperse packing and column. Both columns are $L = 16$ mm in length, $r_c = 0.5$ mm in radius, with an average column-to-particle radius ratio of 10. A void length of $\approx 0.4 r_c$ is present at the ends of the columns. The columns are illustrated in Fig. 3 and their geometrical properties are summarized in Table 2.

Due to current scalability limitations in the simulation toolchain, the geometries are restricted to smaller column diameters and larger particle diameters relative to standard analytical chromatography systems. While microbore columns with 1 mm internal diameter do exist, particle sizes in typical analytical columns are much smaller, in the range of 1.7 µm to 10 µm [22]. Ongoing work is addressing these limitations through software enhancements, the use of anisotropic meshes, and

Table 2
Geometrical properties of random generated packed bed columns.

Particle size distribution	Number of particles	Average particle radius	Column porosity	Bed porosity
Monodisperse	13,845	49.985	0.425	0.411
Polydisperse	9874	53.144	0.425	0.401

the implementation of periodic geometries and boundary conditions to emulate unconfined columns without wall effects.

The HD simulations were performed in two stages: (1) a stationary velocity field was calculated for an incompressible fluid by solving the Stokes equations within the interstitial domain, and (2) the transient mass transport and adsorption equations were subsequently solved in both the interparticle and intraparticle domains, utilizing the previously calculated velocity field. In the flow stage, a parabolic profile was used for the inlet velocity to emulate a fully developed laminar flow profile. The imposition of no-slip boundary conditions on both the particle and wall surfaces effectively simulates interfacial friction, thereby facilitating the development of boundary layers within the flow field.

In the mass transfer stage, an advection–diffusion equation was solved in the bulk domain, while coupled diffusion–adsorption equations were solved in the particle domain. A constant and steady feed concentration of $7.14.10^{-3}$ mol m^{-3} was applied at the inlet. Initial concentrations throughout the entire column were uniformly set to zero in all phases. Mass flux continuity was maintained at the interface of the two domains, that is, the particle surfaces. Adsorption and desorption within the particles were described using the Langmuir model, where the employed parameter values represent the binding behavior of lysozyme on Sepharose particles [23]. Column loading was simulated until full breakthrough, that is, when the outlet concentration equals the inlet concentration.

The simulations were performed on the JURECA supercomputer at Forschungszentrum Jülich using XNS, a massively-parallel multi-physics solver developed at CATS, RWTH Aachen University. Further details regarding the setup and solution of HD simulations can be found in our previous work [19].

5.2. ROM configuration

Setting up ROMs that closely correspond to the HD model described in the previous section requires decisions regarding the representation of several aspects of the column geometry, packing, mass transport, and adsorption process. In this work, the packed bed and the void regions at both ends of the column are compartmentalized as shown in Fig. 4, with each compartment in the figure corresponding to a separate unit operation model in CADET.

Void regions preceding and following the packed bed region in the HD reference geometry are modeled using the lumped rate model without pores (LRM) with a total porosity of one and no dispersion, emulating a plug flow reactor (PFR) without any particles. In this approach, minor dispersive effects due to the velocity boundary region at the column wall are neglected. The constant total flowrate from the HD flow simulations is applied, and the void regions are uniformly discretized using $N_z = 10$ axial elements.

The packed bed region itself is modeled using either the conventional 1D GRM, or the newly implemented 2D GRM. The packed bed region is uniformly discretized axially into $N_z = 100$ elements, and, in 2D cases, radially into $N_\rho = 5$ elements. Geometrical characteristics of the column, including the length, cross section area, and bed porosity, and the related flow velocity are configured based on the corresponding features of the respective reference HD column. For models with PSD, the particles constituting the polydisperse HD packed bed are discretized into N_{bins} bins of equal size $\Delta r = \frac{r_{\max} - r_{\min}}{N_{\text{bins}}}$ as follows.

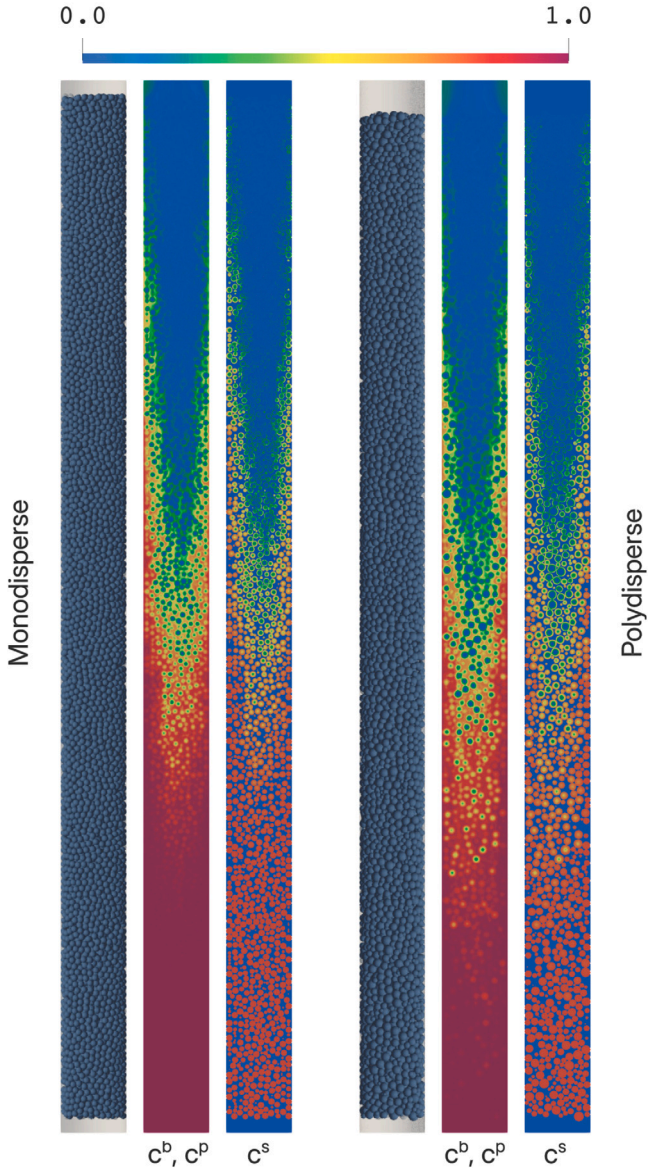

Fig. 3. Geometry and mass transport results of HD monodisperse (left) and polydisperse (right) column simulations at $t = 4550$ s. Liquid phase (c^b, c^p) and solid phase (c^s) results both show pronounced wall effects.

$$B_k = \{i \in \mathcal{P} : r_{\min} + k\Delta r \leq r_i < r_{\min} + (k+1)\Delta r\} \tag{31}$$

where B_k is the kth bin with $k \in \{1, \ldots, N_{\text{bins}}\}$, and $\mathcal{P}$ is the set of all particles in the packed bed. $N_{\text{bins}} = 10$ for all ROMs with PSD in this work. The resulting histogram is shown in Fig. 5(a).

Eq. (32) is applied to the HD geometry and interstitial flow simulation results to reduce, i.e. average, the column porosity and axial flowrates for each radial zone in the 2D GRM. The resulting radial profiles of porosity and velocity for $N_\rho = 5$ are shown in comparison to those obtained with $N_\rho = 40$ with cubic interpolation in Figs. 5(c) and 5(d). Such oscillations in radial profiles of porosity are also reported in the literature [24].

$$u_w = \frac{1}{L} \int_{\rho_{w-\frac{1}{2}}}^{\rho_{w+\frac{1}{2}}} \int_0^{2\pi} \int_0^L u \, dV \qquad \text{in } \Omega_1 \tag{32a}$$

$$\varepsilon_{c,w} = \frac{1}{\pi \cdot (\rho^2_{w+\frac{1}{2}} - \rho^2_{w-\frac{1}{2}}) \cdot L} \int_{\rho_{w-\frac{1}{2}}}^{\rho_{w+\frac{1}{2}}} \int_0^{2\pi} \int_0^L dV \qquad \text{in } \Omega_1 \tag{32b}$$



(a) Compartmentalized unit operation sequence in 1D and 2D GRM

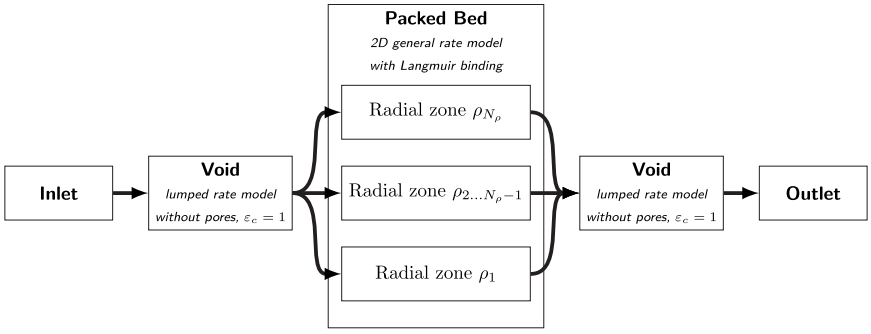

(b) Flow connectivity between unit operations in 2D GRM

Fig. 4. Compartmentalization and flow connectivity in CADET.

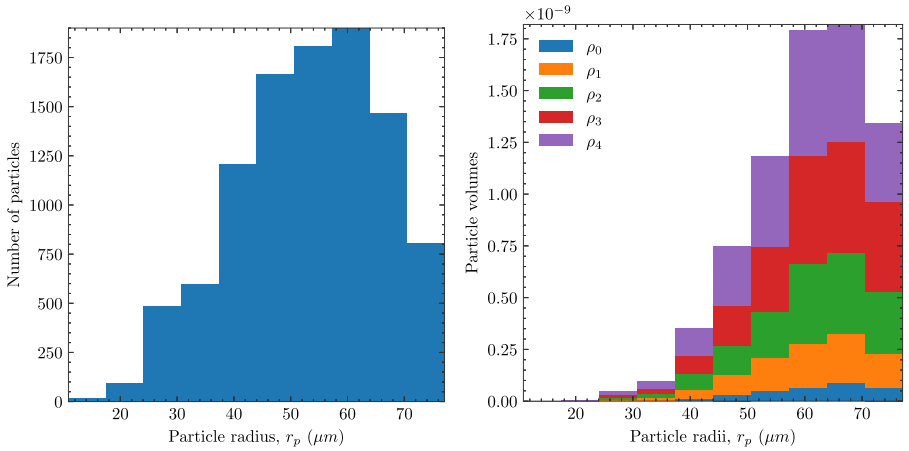

(a) PSD (b) Volume fractions

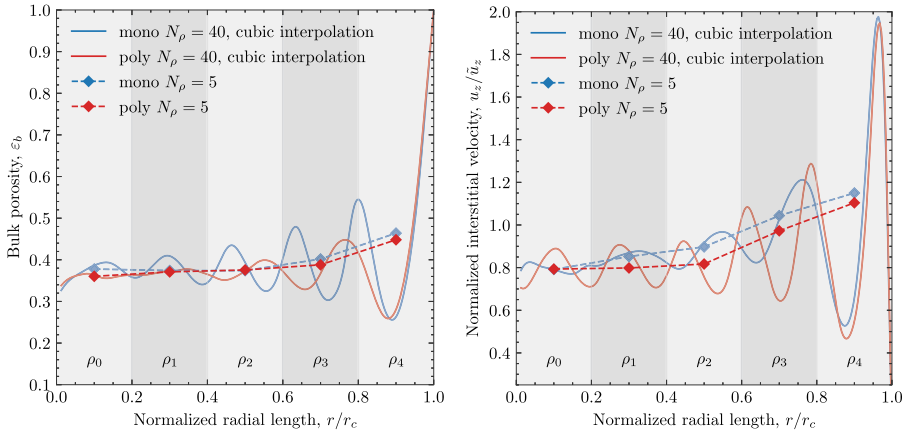

(c) Porosity profiles (d) Velocity profiles

Fig. 5. Geometric inhomogeneities in HD simulated columns.

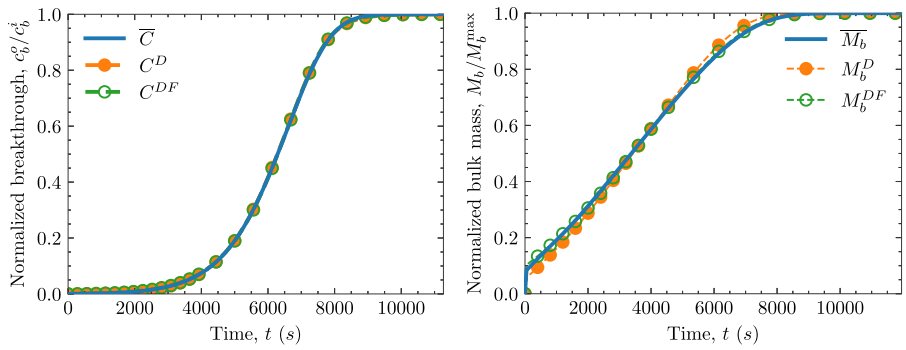

(a) Breakthrough curves (b) Bulk mass curves

Fig. 6. Calibration results for 1D GRM without PSD.

Table 3
Fixed parameters in 1D GRM without PSD.

Parameter	Value
General rate model	
Column length, L	$1.560 \cdot 10^{-2}$ m
Column radius, r_c	$5.01 \cdot 10^{-4}$ m
Particle radius, r_p	$4.999\,85 \cdot 10^{-5}$ m
Particle porosity, ε_p	0.75
Particle diffusion coefficient, D_p	$7.07 \cdot 10^{-11}$ m^2 s^{-1}
Particle surface diffusion, D_s	0.0 m^2 s^{-1}
Langmuir adsorption	
Adsorption coefficient, k_a	1.144 m^3 mol^{-1} s^{-1}
Desorption coefficient, k_d	$2.0 \cdot 10^{-3}$ s^{-1}
Maximum binding capacity, $c^s_{\max}$	4.88 mol m^{-3}
Binding type	kinetic
Discretization	
Column axial discretization, N_z	100
Particle radial discretization. N_r	10

The column radius r_c is discretized into N_ρ radial zones ρ_w, bounded by lower and upper radii $[\rho_{w-\frac{1}{2}}, \rho_{w+\frac{1}{2}}]$, where $w \in \{1, \dots, N_\rho\}$. L represents the length of the packed-bed region of the column.

Surface diffusion is not considered in this work. Other model transport parameters such as film diffusion, axial and radial dispersion coefficients are estimated as specified in the following subsection. Dynamic binding using the Langmuir model with the same parameters as in the reference HD simulations was applied. Table 3 shows the prespecified parameters for a 1D GRM representation of the monodisperse column used in this work.

5.3. Objectives and reference data

Chromatograms are the standard output metric associated with chromatography columns due to their simple representation of the outlet concentration of the column over time, leading to their direct utility in fractionation. Experimentally obtained chromatograms, specifically breakthrough curves, are useful in analyzing the performance of the column and are widely used as data in calibrating ROMs, with several studies on the effects of various intra-column phenomena on breakthrough curves. However, these curves are just reduced, i.e. averaged, solute concentrations at only the column outlet. These single curves are not sufficiently unique descriptors of the internal state of the column. This can be illustrated by the following example with two 1D GRM ROMs, the first (model D) without thin-film resistance, i.e., $k_f = \infty$, where D_{ax} is the only calibration parameter, and the second (model DF) with both D_{ax} and k_f as finite calibration parameters. When using the 1D breakthrough curve as the objective, both models result in seemingly perfect fits to the reference data (Fig. 6(a)).

The reason for this behavior is that both the thin-film resistance and the axial dispersion phenomena result in a band-broadening effect on the chromatogram, and compensate for each other's effect on the breakthrough curve in the calibration process. Although the fit with respect to reference data in both models is excellent, resulting in identical column outputs, the internal states of the columns in the two models are distinctly different due to fundamentally differing mechanisms being calibrated to different degrees.

On the other hand, solute masses in each phase (M_b, M_p, and M_s; Eq. (33)) are unique representations of the internal state of the column. Fig. 6(b) shows that both models D and DF produce disparate fits when calibrating them using the reduced solute bulk mass M_b, with model DF resulting in a better fit.

$$M_b = \int_{\Omega_1} c^b \, dV \tag{33a}$$

$$M_p = \int_{\Omega_2} \varepsilon_p c^p \, dV \tag{33b}$$

$$M_s = \int_{\Omega_2} (1-\varepsilon_p) c^s \, dV \tag{33c}$$

In this work, we utilize M_b, M_p, and M_s as objectives. Using all the phase masses in combination allows the optimizer to account for the mass balance within the ROM column, resulting in calibrated ROMs that more closely approximate the reference column.

Reference data for the selected objectives are generated by reducing HD simulation results to match the dimensionality and discretization scheme applied to the ROM. In this work, as per convention, we further spatially average the calibration reference data in the axial dimension. Thus, in calibrating 2D GRM, our process results in N_ρ objectives per phase.

The reduced solute masses in each phase, $\overline{M}_b$, $\overline{M}_p$, and $\overline{M}_s$, used as reference data for the objectives in the ROM calibration are calculated as follows in Eq. (34).

$$\overline{M}_b^w = \int_{\rho_{w-\frac{1}{2}}}^{\rho_{w+\frac{1}{2}}} \int_0^{2\pi} \int_0^L c^b \, dV \qquad \forall w \in \{1, \dots, N_\rho\} \quad \text{in } \Omega_1 \tag{34a}$$

$$\overline{M}_p^w = \int_{\rho_{w-\frac{1}{2}}}^{\rho_{w+\frac{1}{2}}} \int_0^{2\pi} \int_0^L \varepsilon_p \, c^p \, dV \qquad \forall w \in \{1, \dots, N_\rho\} \quad \text{in } \Omega_2 \tag{34b}$$

$$\overline{M}_s^w = \int_{\rho_{w-\frac{1}{2}}}^{\rho_{w+\frac{1}{2}}} \int_0^{2\pi} \int_0^L (1-\varepsilon_p) c^s \, dV \qquad \forall w \in \{1, \dots, N_\rho\} \quad \text{in } \Omega_2 \tag{34c}$$

where the column radius r_c is discretized into N_ρ radial zones ρ_w, bounded by lower and upper radii $[\rho_{w-\frac{1}{2}}, \rho_{w+\frac{1}{2}}]$ with $w \in \{1, \dots, N_\rho\}$.

The range-normalized root mean square error (NRMSE, Eq. (35)) is used as scoring function for each objective. This normalization effectively assigned identical weights to each objective, thereby eliminating any bias associated with differences in their original magnitude in the reference data.

$$\xi_\kappa^w = \frac{\sqrt{\frac{1}{N_t}(\overline{M}_\kappa^w - M_\kappa^w)^2}}{\max(\overline{M}_\kappa^w) - \min(\overline{M}_\kappa^w)} \quad \forall \kappa \in \{b, p, s\}, \forall w \in \{1, \dots, N_\rho\} \tag{35}$$

where N_t is the number of discretization in time, κ is the phase index, and w is the index of the radial zone.

5.4. Parameters

D_{ax}, D_ρ, and k_f are considered as calibration parameters, while all other parameters of the ROM are pre-determined. In 1D GRM, we have D_{ax} and k_f as scalar values to calibrate, whereas in 2D GRM we have N_ρ axial and radial dispersion coefficients in addition to k_f calibration parameters, assuming only radial dependence of such parameters.

While specific lower and upper bounds were applied to the parameters during calibration ($D_{\text{ax}}, D_\rho \in [1 \times 10^{-9}, 1 \times 10^{-5}]$, and $k_f \in [1 \times 10^{-8}, 1 \times 10^{3}]$), these constraints effectively represented no limitations on the true solution space for the chosen case studies. As velocities and porosities remain fairly constant in the first 3 radial zones as shown in Figs. 5(c) and 5(d), we constrain corresponding dispersion coefficients in these zones to the same value in order to avoid overfitting the data and reduce the number of calibration parameters. To facilitate faster convergence, the calibration parameters were first transformed into logarithmic space (log10) and then normalized across their respective ranges.

5.5. Algorithm

The calibrations in this work were performed using the genetic algorithm UNSGA-III, due to its robustness in multi-objective, multi-parameter problems. The initial population was generated using a Sobol sequence, a specifically designed low-discrepancy sequence capable of efficiently sampling and spanning the entire high-dimensional parameter space. Initialization with low-discrepancy sequences leads to better exploration of the parameter space, leading to potentially faster convergence rates [25].

5.6. Multi-criteria decision making

Multi-objective optimizations result in a set of optimal or near-optimal solutions that span a multi-dimensional surface in the objective space known as the Pareto front, which represents trade-offs between individual solutions for specific objectives. This span can be visualized for every objective in the calibration process, and is denoted in this work as $\langle M_\kappa^w \rangle$. It provides information about the range of the Pareto front in the objective space.

In order to find the best solution in the optimal set, we scalarize the multiple residuals ξ_κ^w using the root mean square (RMS) function as shown in Eq. (36), and pick the solution with the least scalarized (meta-)residual $\tilde{\xi}$.

$$\tilde{\xi} = \sqrt{\frac{1}{N_\xi} \sum_\kappa \sum_{w=1}^{N_\rho} (\xi_\kappa^w)^2} \tag{36}$$

where $N_\xi = N_\Phi \cdot N_\rho$ is the number of total objectives, with N_Φ and N_ρ representing the number of phases and radial zones respectively considered in the calibration process.

The best fitting objectives $\widehat{M}_\kappa^w$ are selected such that they minimize $\tilde{\xi}$, i.e., $\widehat{M}_\kappa^w = \arg\min \tilde{\xi}$. The corresponding best-fit parameters are notated as $\widehat{D}_{\text{ax}}^w$, $\widehat{D}_\rho^w$, and $\widehat{k}_f$.

While it is also possible to directly use the scalarized metric as the only optimization objective, formulating the parameter estimation as a multi-objective problem results in the optimizer taking into account the individual sensitivities of every objective with respect to every parameter. Furthermore, multi-objective optimization leads to better exploration of the objective space, thus resulting in more comprehensive information for decision making.

The optimization itself is terminated upon convergence of the meta-residual and every parameter for the median and best individual solutions in every generation is manually verified. While limits can be placed upon the number of ROM evaluations or generations, allowing the optimizer to proceed by visual inspection of the meta-residual allows to refine the optimal solution set further until the parameters fully converge and patterns emerge.

6. Results and discussions

6.1. Breakthrough curves vs. solute mass curves

Table 4 shows the results of calibrating 1D ROMs with and without PSD against the corresponding case study geometries and HD results using either breakthrough curves or bulk mass curves as reference data. While all calibrations show similarity in the NRMSE ξ, indicating convergence, the resulting parameters for calibrations derived from breakthrough curves show strong deviations from expected values. The chromatogram-based calibrations either underestimate D_{ax} or overestimate k_f, a consequence of the system being unable to simultaneously resolve the dispersive effects of the two parameters on the breakthrough curve. In contrast, calibrations based on bulk mass curves result in reasonable values of both D_{ax} and k_f.

6.2. Effect of polydispersity

We analyze the effect of neglecting PSD and using only the average particle size in modeling chromatography using the conventional 1D GRM. Two ROMs are calibrated to the results of the HD polydisperse column: (a) GRM without PSD, and (b) GRM with PSD. Both D_{ax} and k_f are used as calibration parameters, with M_b as reference data.

Modeling a polydisperse packing using only the average particle size leads to, among other effects, neglecting the effects of the packed bed surface area and volume on the column results. For instance, the size of the flow boundary region at particle surfaces responsible for the thin-film resistance is dependent on the surface area of the packed bed. This boundary region also contributes to axial dispersion within the column. As shown in Table 5, using the ROM without PSD for the polydisperse packing resulted in 37% reduction in k_f in order to compensate for the 10% increase in the packed-bed surface area, keeping the total mass transfer across the bulk and particle domains constant while fitting to reference data. Coefficient of axial dispersion was reduced by 5%. The bed surface area was calculated using the 3D polydisperse packing for the model with PSD, and recalculated for the model without PSD assuming all particles had their size equal to the average size in the packing.

Fig. 7 shows the fit plots for the two calibrations, with both models being able to adjust their parameters to obtain a good fit. In effect, the changes in the calibration parameters compensate for the effects of polydispersity.

6.3. All phase masses as objectives

The bulk phase mass, M_b is sufficient as an objective metric for our case study as all the optimization parameters D_{ax}, D_ρ, and k_f are based on transport phenomena in the bulk domain. However, using solute masses in the particle pore phase M_p, and stationary phase M_s as additional objectives provides a multi-faceted view of the transport

Table 4
Calibration results with breakthrough curves (C) and bulk solute mass (M_b) as reference data. Due to overlapping dispersive effects on C, the parameter estimation process cannot reliably fit both D_{ax} and k_f concurrently.

Packing type		Axial dispersion	Film diffusion	Residual
HD	ROM	D_{ax} ($m^2\,s^{-1}$)	k_f ($m\,s^{-1}$)	ξ
Breakthrough curves C as reference data				
Monodisperse	Without PSD	$7.72 \cdot 10^{-7}$	$9.98 \cdot 10^{2}$	$4.01 \cdot 10^{-3}$
Polydisperse	With PSD	$4.11 \cdot 10^{-9}$	$6.42 \cdot 10^{-6}$	$5.37 \cdot 10^{-3}$
Bulk solute mass M_b as reference data				
Monodisperse	Without PSD	$4.75 \cdot 10^{-7}$	$8.09 \cdot 10^{-6}$	$5.41 \cdot 10^{-3}$
Polydisperse	With PSD	$3.30 \cdot 10^{-7}$	$7.18 \cdot 10^{-6}$	$5.87 \cdot 10^{-3}$

Table 5
Effect of neglecting PSD on D_{ax} and k_f in 1D GRM.

Packing type		Packed-bed surface area (m^2)	Axial dispersion D_{ax} ($m^2\,s^{-1}$)	Film diffusion k_f ($m\,s^{-1}$)
HD	ROM			
Polydisperse	Without PSD	$4.09 \cdot 10^{-4}$	$3.11 \cdot 10^{-7}$	$4.40 \cdot 10^{-6}$
Polydisperse	With PSD	$3.70 \cdot 10^{-4}$	$3.30 \cdot 10^{-7}$	$7.18 \cdot 10^{-6}$

Table 6
Comparison of k_f values fitted using ROMs vs. empirical correlations.

Packing type	ROM	Simulation fit	Wilson-Geankoplis	Kataoka	Penetration correlation
HD mono	1D mono	$8.10 \cdot 10^{-6}$	$1.25 \cdot 10^{-5}$	$1.00 \cdot 10^{-5}$	$1.74 \cdot 10^{-5}$
	2D mono	$1.36 \cdot 10^{-5}$			
HD poly	1D poly	$6.85 \cdot 10^{-6}$	$1.23 \cdot 10^{-5}$	$9.75 \cdot 10^{-6}$	$1.69 \cdot 10^{-5}$
	2D poly	$5.49 \cdot 10^{-6}$			

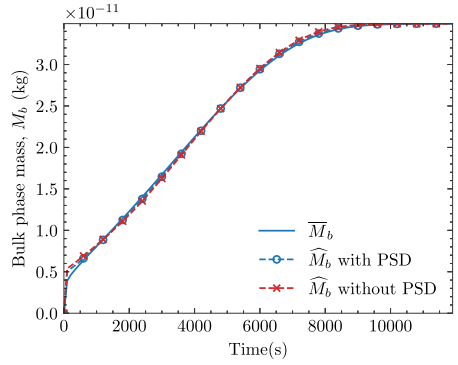

Fig. 7. Optimal fits obtained while calibrating 1D GRM with and without PSD against bulk phase mass (M_b) for HD polydisperse packing.

processes and enables visualizing the differences in the HD model and the GRM.

Fig. 8 shows the span of the optimal solutions $\langle M_\kappa \rangle$, the best fit with the least scalarized error $\widehat{M}_\kappa$, and the reference curve $\overline{M}_\kappa$ for objectives $M_\kappa \forall \kappa \in \{b, p, s\}$ for the 1D GRM with and without PSD. The model with PSD clearly performs better than the model without PSD, with narrower spans for all objectives. The best fit $\widehat{M}_b$ is indistinguishable from the reference curve $\overline{M}_b$, while $\widehat{M}_p$ and $\widehat{M}_s$ show slight discrepancies with respect to their corresponding reference curves. These discrepancies are most likely the result of incompatibilities between the HD model and ROM setup for the given case study. This will be discussed in more detail in the upcoming subsection.

Fig. 9, showing all simulation evaluations plotted on each combination of objectives and parameters as plot axes, provides additional context to the fit plot. As expected, M_b is highly responsive to both model parameters, while M_p and M_s are not completely congruent with M_b.

6.4. Radial inhomogeneity

In this subsection, we exhibit results of calibration of a 2D GRM representation of our reference column with axial dispersion (D_{ax}), radial dispersion (D_ρ), and film diffusion (k_f) coefficients based on HD results. The column is divided into $N_\rho = 5$ equidistant, radially concentric zones where the local values of porosity, axial velocity, and internal masses for each of these zones are calculated from the HD geometry and simulation results. This discretization is the finest possible while keeping radial zone widths not smaller than particle sizes. Reduced porosity and velocity profiles along with the PSD are shown in Fig. 5.

Table 6 shows the best calibrated values of film diffusion coefficients for the models with respect to three empirical correlations. Calibrations of 2D GRM with and without PSD were performed against the corresponding HD reference data. Fig. 10 shows the span of predictions for the Pareto front $\langle M_\kappa^w \rangle$, and the best prediction $\widehat{M}_\kappa^w$, against the corresponding reference curves, $\overline{M}_\kappa^w$, where $w \in \{1, \ldots, N_\rho\}$ and $\kappa \in \{b, p, s\}$ for all objectives.

The ROM with PSD performed significantly better than the one without PSD in all objectives, displaying much narrower spans for every objective. The latter is most likely due to the still-significant oscillation in porosity and velocity profiles in the monodisperse packing at the column center, which is antithetical to the assumption of homogeneity within each radial element in ROMs. Polydisperse packings, on the other hand, tend to attain homogeneity in the radial porosity profile towards the column center at a faster rate due to the heterogeneously sized particles being able to fill the interstitial spaces more effectively. GRM with PSD can also account for different size distributions in different radial zones.

Furthermore, the process of generating reduced reference data from HD simulations based on the radial discretization scheme applied to the ROM involves "splitting" particles that cross the boundaries of 2D radial zones. While the HD simulation considers the particle whole and implicitly models the effects of the packed-bed volume and surface area on interstitial flow, the ROM assumes them to be separate particles in separate radial zones with no transport or adsorption between them. GRM with PSD performs better in this regard as the model can account

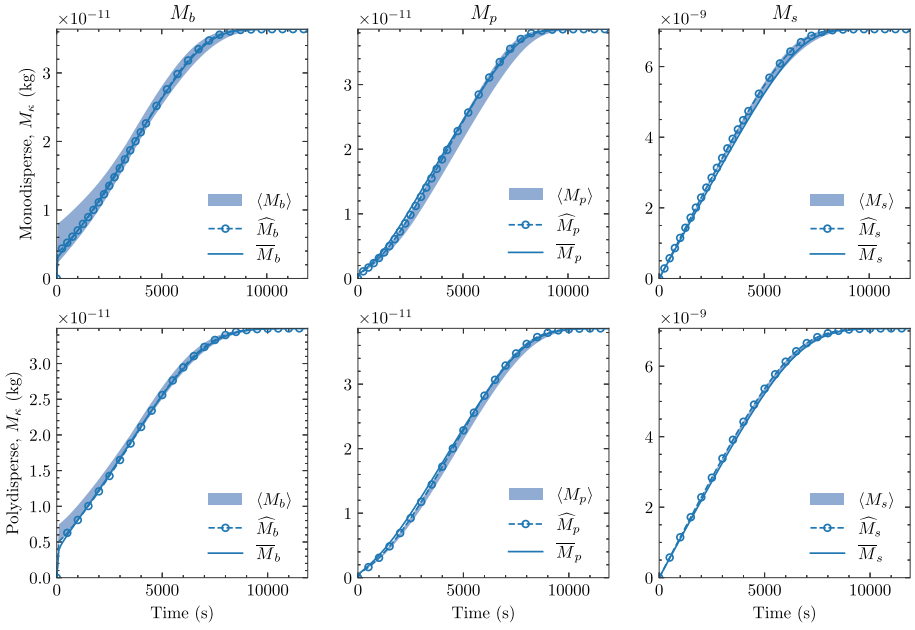

Fig. 8. Plots showing the spans of Pareto front ($\langle M_\kappa \rangle$), best fit ($\widehat{M}_\kappa$), and reference curve ($\overline{M}_\kappa$) for the 1D GRM calibrations; without PSD for the monodisperse case (top), and with PSD for the polydisperse case (bottom). Thinner spans in the polydisperse case indicate better compatibility between the reference data and the ROM with PSD, leading to better match between $\overline{M}_\kappa$ and $\widehat{M}_\kappa$.

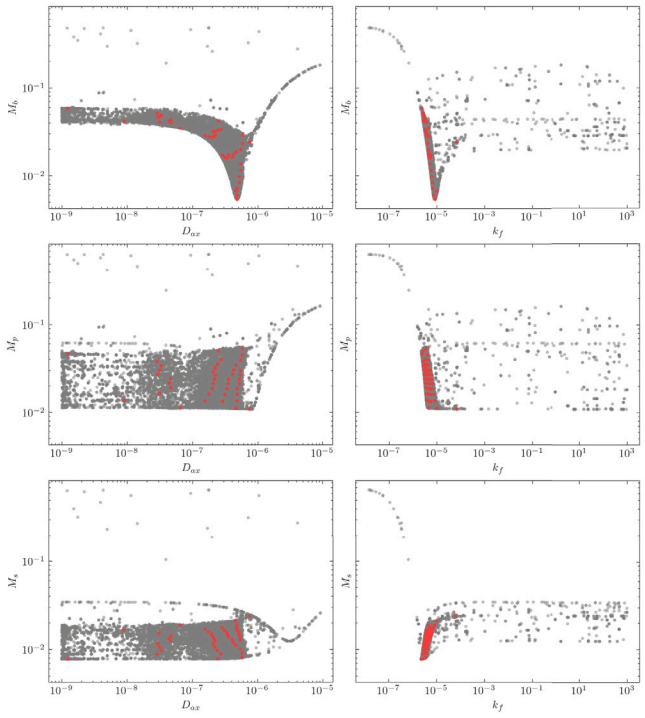

Fig. 9. All combinations of parameters vs. objectives for all ROM evaluations in the 1D GRM calibration without PSD. Pareto optimal solutions are marked in red.

for exact volume fractions and radii of such particles in each radial zone.

While it can be argued that a finer radial discretization is necessary to capture high degrees of radial variation in parameters, it would also cause particle sizes to be larger than the size of the radial zone, violating another aspect of the homogeneity assumptions in ROMs. This would also exacerbate the disparity between the HD model and ROMs with respect to the "splitting" of particles at radial zone boundaries.

It is again observed that both models performed better with the bulk (M_b) and particle (M_p) domain objectives in comparison to those in the solid (M_s) domain. This can be attributed to the fact that the calibration parameters D_{ax}, k_f are linked to phenomena occurring primarily in the bulk domain or the interface between the bulk and particle domains D_{ax} acting entirely in the bulk domain, and k_f acting on the interface between the bulk and particle domains.

7. Conclusions

A novel implementation of the 2D General Rate Model (GRM) developed for the open-source process simulator CADET-Core was calibrated using results from high-definition (HD) three-dimensional spatially-resolved simulations of packed-bed chromatography. The increased dimensionality in 2D GRM supports higher model fidelity in comparison to conventional 1D models. Specifically, radially variable parameters enable capturing local variations in porosity, and flowrates, which, in turn, allows modeling wall effects and packing defects in a more mechanistic manner without lumping their effects into axial and radial dispersion coefficients. 1D/2D GRM in CADET-Core can also model columns with particle size distributions (PSD).

However, the benefits of increased fidelity are counterbalanced by the limitations of the reduced-order model. The increased dimensionality also leads to a multiplicative increase in the number of tunable dispersion coefficients, $2N_\rho$ in 2D GRM (where N_ρ is the discretization in the radial dimension) against the singular axial dispersion coefficient in 1D models. While 1D models could be simulated with a constant scalar porosity and flowrate, 2D models require not only the radially varying porosity data, but also the corresponding flowrates. Consequently, calibration of such a model necessitates spatially-resolved reference data and a multi-objective approach to parameter estimation. The higher computational expense in comparison to conventional 1D models also compounds the time required to calibrate the 2D GRM.

High-definition (HD) geometry and simulation results from a previous work were post-processed to generate such reference data and pre-determined parameters for model calibration. HD geometry consists of 3D column geometry with a fully resolved packed-bed and interstitial geometry at a macroscopic level. Two hypothetical micro-columns with

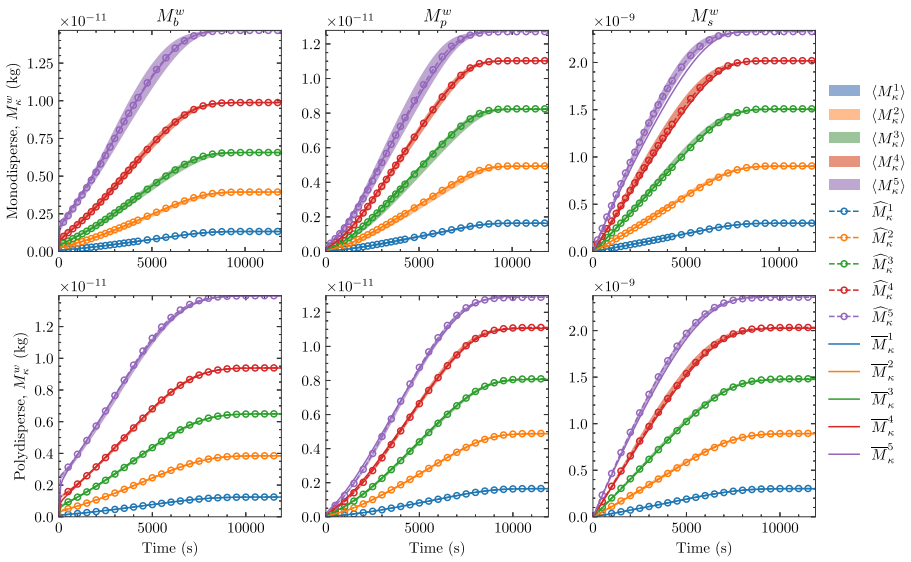

Fig. 10. Spans of the Pareto front for the 2D GRM calibrations in the monodisperse (top) and polydisperse (bottom) cases.

identical container dimensions and differing packed-beds were considered for this work; one column with 13,845 single-sized (monodisperse) particles, and the other consisting of 9874 particles with a specified size distribution (polydisperse). While the column size, number of particles, and the column-to-particle radius ratio ($\frac{r_c}{r_p} \approx 10$) are not reflective of commercially available microcolumns, this setup was sufficient in order to demonstrate the modeling of wall effects and dispersive processes.

Compartmentalized 1D and 2D GRM representations of the reference column were calibrated under breakthrough conditions. Prespecified ROM parameters and reference data for the calibrations were reduced from the reference HD geometry and simulations. It was shown that solute masses for the bulk M_b, particle pore M_p, and solid M_s phases served as more suitable objectives compared to the conventionally used breakthrough curves. The use of solute mass curves in ROM calibration resulted in disparate fit plots for models with infinite and finite film diffusion coefficient k_f, whereas both models resulted in indistinguishable fits with breakthrough curves as objectives. Furthermore, it was observed that breakthrough curves were insufficient to resolve dispersive effects associated with the axial dispersion coefficient and film diffusion coefficient. Utilizing mass curves also allows the calibration process to account for mass balance across different phases within the column, resulting in more reliable estimations of the film diffusion and dispersion coefficients.

It was observed that models with PSD performed better than their conventional counterparts for the thin column geometries in our case study. Polydisperse packings by nature of their heterogeneity in particle sizes are able to achieve a more uniform local porosity away from the column walls, whereas monodisperse packings still exhibit oscillations in local porosity due to the constant-sized particles. Furthermore, models with PSD in CADET are able to capture varying particle size distributions across radial zones, which results in a closer fit with the reduced HD reference data for our case study.

Neglecting the polydispersity of the column in the studied case resulted in a 37% reduction in the estimated film-diffusion coefficient and only a 5% reduction in the axial dispersion coefficient in 1D GRM. As the size and surface area of individual particles contribute strongly to the total volume of boundary layer region developed in the column bulk, the loss of this information when using monodisperse models on columns with PSD leads to a miscalibration.

All in all, although thin columns with large particle sizes are not ideally simulated with conventional ROMs due to their implicit assumptions of homogeneity, we show that models with PSD, both 1D and 2D, are able to sufficiently and accurately capture the internal state of the reference column when calibrated with respect to internal solute masses in every phase. Additional improvements to the ROM setup in this work are, however, possible. The PSD discretization could be subject to further refinement, the film diffusion coefficient could be varied based on particle size, and a finite dispersion in the void regions could also be considered.

Although this work focuses on thin columns with strong wall effects, we hypothesize that the impact of PSD is still substantial in much wider columns. While it is infeasible to directly scale existing confined-geometry HD simulations to a point where wall effects can be completely neglected, an alternative approach to simulate wider columns and unconfined packings using laterally periodic boundary conditions is currently being developed. In future works, we aim to investigate and isolate the effects of individual geometrical factors such as wall effects, imperfect flow distribution at the inlet, PSD, and particle morphology on dispersion coefficients and mass transfer coefficients in ROMs.

Computational efficiency is particularly critical for the 2D GRM, as employing multiple radial zones and/or a particle size distribution can quickly increase the computational burden. The implementation of high-order or arbitrary-order numerical methods (Discontinuous Galerkin Spectral Element Methods) for 1D chromatography models in CADET have provided tremendous gains in computational efficiency [26]. Future work will focus on extending the existing spectral methods in CADET to include the 2D GRM, specifically to the governing equations that involve radial geometry with radially dependent parameters. Since the performance increase is positively correlated with the problem size, we anticipate an even greater performance improvement than what was achieved for the 1D models.

CRediT authorship contribution statement

Jayghosh Subodh Rao: Writing – original draft, Visualization, Validation, Software, Methodology, Investigation, Formal analysis, Data curation, Conceptualization. **Samuel Leweke:** Writing – original draft, Software, Methodology, Conceptualization. **Jan Michael Breuer:** Writing – original draft, Visualization, Validation, Software, Methodology, Investigation, Formal analysis, Data curation, Conceptualization. **Stephan Menzel:** Resources, Conceptualization, Supervision. **Marek Behr:** Writing – review & editing, Supervision, Project administration, Funding acquisition. **Eric von Lieres:** Writing – review & editing, Supervision, Resources, Project administration, Methodology, Funding acquisition, Conceptualization.

Declaration of competing interest

The authors declare that they have no known competing financial interests or personal relationships that could have appeared to influence the work reported in this paper.

Acknowledgments

The HD simulation and ROM calibration were conducted during the Ph.D. study of Jayghosh Rao. The authors gratefully acknowledge the funding and support of the JARA-SSD program, as well as the computing time granted through JARA on the supercomputer JURECA [27,28] at Forschungszentrum Jülich. Jan M. Breuer has received funding by the Deutsche Forschungsgemeinschaft, Germany (DFG, German Research Foundation) – 548805630 (grant no. GA 2160/8-1). The authors gratefully acknowledge scientific discussions with Stephan Menzel and Gunnar Malmquist, and funding of the CADET extension provided by GE Healthcare (now Cytiva). The three-dimensional packings used in this work were computationally generated by the team of Ulrich Tallarek at the Department of Chemistry, Philipps-University, Marburg. Joel Andersson, Sebastian Schnittert, and Andreas Püttmann have made substantial contributions to earlier versions of CADET-Core [8,12,13,29].

Appendix A. Supplementary data

Supplementary material related to this article can be found online at https://doi.org/10.1016/j.seppur.2025.134409.

Data availability

Data will be made available on request.

References

[1] G. Guiochon, A. Felinger, D.G. Shirazi, A.M. Katti, Fundamentals of Preparative and Nonlinear Chromatography, second ed., Elsevier Academic Press, Amsterdam, 2006.
[2] A. Höltzel, U. Tallarek, S. Bruns, Morphological comparison of silica-based monolithic and particulate beds by confocal laser scanning microscopy, 2013.
[3] G. Zhao, L. Zhang, S. Bai, Y. Sun, Analysis of hydrophobic charge induction displacement chromatography by visualization with confocal laser scanning microscopy, Sep. Purif. Technol. 82 (2011) 138–147, http://dx.doi.org/10.1016/j.seppur.2011.09.002.
[4] I. Langmuir, The adsorption of gases on plane surfaces of glass, Mica Platin. J. Am. Chem. Soc. 40 (1918) 1361–1403, http://dx.doi.org/10.1021/ja02242a004.
[5] P. Danckwerts, Continuous flow systems: Distribution of residence times, Chem. Eng. Sci. 2 (1953) 1–13, http://dx.doi.org/10.1016/0009-2509(53)80001-1, URL http://linkinghub.elsevier.com/retrieve/pii/0009250953800011.
[6] S. Qamar, D.U. Uche, F.U. Khan, A. Seidel-Morgenstern, Analysis of linear two-dimensional general rate model for chromatographic columns of cylindrical geometry, J. Chromatogr. A 1496 (2017) 92–104, http://dx.doi.org/10.1016/j.chroma.2017.03.048.
[7] G. Carta, A. Ubiera, Particle-size distribution effects in batch adsorption, AIChE J. 49 (2003) 3066–3073, http://dx.doi.org/10.1002/aic.690491208.
[8] E. von Lieres, J. Andersson, A fast and accurate solver for the general rate model of column liquid chromatography, Comput. Chem. Eng. 34 (2010) 1180–1191, http://dx.doi.org/10.1016/j.compchemeng.2010.03.008.
[9] S. Leweke, J. Breuer, J. Schmölder, R. Jäpel, H. Lanzrath, J. Rao, J. Hassan, W. Zhang, A. Berger, W. Heymann, E. von Lieres, Cadet-core: Version 5.0.3, 2024, http://dx.doi.org/10.5281/zenodo.14419680.
[10] D.J. Gardner, D.R. Reynolds, C.S. Woodward, C.J. Balos, Enabling new flexibility in the SUNDIALS suite of nonlinear and differential/algebraic equation solvers, ACM Trans. Math. Softw. (TOMS) 48 (2022) 1–24, http://dx.doi.org/10.1145/3539801.
[11] A.C. Hindmarsh, P.N. Brown, K.E. Grant, S.L. Lee, R. Serban, D.E. Shumaker, C.S. Woodward, SUNDIALS: Suite of nonlinear and differential/algebraic equation solvers, ACM Trans. Math. Softw. (TOMS) 31 (2005) 363–396, http://dx.doi.org/10.1145/1089014.1089020.
[12] A. Püttmann, S. Schnittert, S. Leweke, E. von Lieres, Utilizing algorithmic differentiation to efficiently compute chromatograms and parameter sensitivities, Chem. Eng. Sci. 139 (2016) 152–162, http://dx.doi.org/10.1016/j.ces.2015.08.050.
[13] A. Püttmann, S. Schnittert, U. Naumann, E. von Lieres, Fast and accurate parameter sensitivities for the general rate model of column liquid chromatography, Comput. Chem. Eng. 56 (2013) 46–57, http://dx.doi.org/10.1016/j.compchemeng.2013.04.021.
[14] S. Leweke, E. von Lieres, Fast arbitrary order moments and arbitrary precision solution of the general rate model of column liquid chromatography with linear isotherm, Comput. Chem. Eng. 84 (2016) 350–362, http://dx.doi.org/10.1016/j.compchemeng.2015.09.009.
[15] S. Leweke, Cadet-semi-analytic, 2024, http://dx.doi.org/10.5281/zenodo.14066869.
[16] J. Breuer, R. Jäpel, Cadet-verification: Version 0.1.0, 2025, http://dx.doi.org/10.5281/zenodo.14594719.
[17] J. Rao, Cadet/cadet-hd-chromoo: v0.2.0, 2025, http://dx.doi.org/10.5281/zenodo.14969179.
[18] Blank J., K. Deb, Pymoo: Multi-objective optimization in python, IEEE Access 8 (2020) 89497–89509.
[19] J.S. Rao, A. Püttmann, S. Khirevich, U. Tallarek, C. Geuzaine, M. Behr, E. von Lieres, High-definition simulation of packed-bed liquid chromatography, Comput. Chem. Eng. 178 (2023) 108355, http://dx.doi.org/10.1016/j.compchemeng.2023.108355, URL https://www.sciencedirect.com/science/article/pii/S0098135423002259.
[20] S. Khirevich, A. Höltzel, D. Hlushkou, U. Tallarek, Impact of conduit geometry and bed porosity on flow and dispersion in noncylindrical sphere packings, Anal. Chem. 79 (2007) 9340–9349, http://dx.doi.org/10.1021/ac071428k.
[21] W.S. Jodrey, E.M. Tory, Computer simulation of close random packing of equal spheres, Phys. Rev. A 32 (1985) 2347–2351, http://dx.doi.org/10.1103/physreva.32.2347.
[22] S.C. Moldoveanu, V. David, Progress in technology of the chromatographic columns in hplc, in: S.C. Moldoveanu, V. David (Eds.), Analytical Liquid Chromatography Chapter 1, IntechOpen, Rijeka, 2022, http://dx.doi.org/10.5772/intechopen.104123.
[23] R.M. Montesinos, A. Tejeda-Mansir, R. Guzmán, J. Ortega, W.E. Schiesser, Analysis and simulation of frontal affinity chromatography of proteins, Sep. Purif. Technol. 42 (2005) 75–84, http://dx.doi.org/10.1016/j.seppur.2004.03.014.
[24] S. Bruns, E.G. Franklin, J.P. Grinias, J.M. Godinho, J.W. Jorgenson, U. Tallarek, Slurry concentration effects on the bed morphology and separation efficiency of capillaries packed with sub-2μm particles, J. Chromatogr. A 1318 (2013) 189–197, http://dx.doi.org/10.1016/j.chroma.2013.10.017, URL https://www.sciencedirect.com/science/article/pii/S0021967313016178.
[25] W.H. Bangyal, K. Nisar, A.A.B. Ag. Ibrahim, M.R. Haque, J.J.P.C. Rodrigues, D.B. Rawat, Comparative analysis of low discrepancy sequence-based initialization approaches using population-based algorithms for solving the global optimization problems, Appl. Sci. 11 (7591) (2021) http://dx.doi.org/10.3390/app11167591.
[26] J.M. Breuer, S. Leweke, J. Schmölder, G. Gassner, E. von Lieres, Spatial discontinuous galerkin spectral element method for a family of chromatography models in cadet, Comput. Chem. Eng. 177 (2023) 108340, http://dx.doi.org/10.1016/j.compchemeng.2023.108340, URL https://www.sciencedirect.com/science/article/pii/S0098135423002107.
[27] Jülich Supercomputing Centre, JURECA: Modular supercomputer at jülich supercomputing centre, J. Large-Scale Res. Facil. 4 (2018) http://dx.doi.org/10.17815/jlsrf-4-121-1.
[28] Jülich Supercomputing Centre, JURECA: Data centric and booster modules implementing the modular supercomputing architecture at jülich supercomputing centre, J. Large-Scale Res. Facil. 7 (2021) http://dx.doi.org/10.17815/jlsrf-7-182.
[29] S. Leweke, E. von Lieres, Chromatography analysis and design toolkit (CADET), Comput. Chem. Eng. 113 (2018) 274–294, http://dx.doi.org/10.1016/j.compchemeng.2018.02.025.